

1 Neutral atmosphere temperature trends and variability at 90 2 km, 70°N, 19°E, 2003-2014

3

4 S. E. Holmen¹²³, C. M. Hall² and M. Tsutsumi⁴⁵

5 [1]{The University Centre in Svalbard, Longyearbyen, Norway}

6 [2]{Tromsø Geophysical Observatory, UiT – The Arctic University of Norway, Tromsø,
7 Norway}

8 [3]{Birkeland Centre for Space Science, Bergen, Norway}

9 [4]{National Institute of Polar Research, Tokyo, Japan}

10 [5]{The Graduate University for Advanced Studies (SOKENDAI), Department of Polar
11 Science, Japan}

12 Correspondence to: S. E. Holmen (siljeh@unis.no)

13

14 Abstract

15 Neutral temperatures at 90 km height above Tromsø, Norway, have been determined using
16 ambipolar diffusion coefficients calculated from meteor echo fading times using the
17 Nippon/Norway Tromsø Meteor Radar (NTMR). Daily temperature averages have been
18 calculated from November 2003 to October 2014 and calibrated against temperature
19 measurements from the Microwave Limb Sounder (MLS) on board Aura. Large-scale
20 periodic oscillations ranging from ~9 days to a year were found in the data using Lomb-
21 Scargle periodogram analysis, and these components were used to seasonally de-trend the
22 daily temperature values before assessing trends. Harmonic oscillations found are associated
23 with the large-scale circulation in the middle atmosphere together with planetary and gravity
24 wave activity. The overall temperature change from 2003 to 2014 is $-2.2 \text{ K} \pm 1.0 \text{ K/decade}$,
25 while in summer (May-June-July) and winter (November-December-January) the change is -
26 $0.3 \text{ K} \pm 3.1 \text{ K/decade}$ and $-11.6 \text{ K} \pm 4.1 \text{ K/decade}$, respectively. The temperature record is at
27 this point too short for incorporating response to solar variability in the trend. How well suited
28 a meteor radar is for estimating neutral temperatures at 90 km using meteor trail echoes is
29 discussed, and physical explanations behind a cooling trend are proposed.

1 **1 Introduction**

2 Temperature changes in the mesosphere and lower thermosphere (MLT) region due to both
3 natural and anthropogenic variations cannot be assessed without understanding the dynamical,
4 radiative and chemical couplings between the different atmospheric layers. Processes
5 responsible for heating and cooling in the MLT region are many. Absorption of UV by O₃ and
6 O₂ causes heating, while CO₂ causes strong radiative cooling. Planetary waves (PWs) and
7 gravity waves (GWs) break and deposit heat and momentum into the middle atmosphere and
8 influence the mesospheric residual circulation, which is the summer-to-winter circulation in
9 the mesosphere. Also, heat is transported through advection and adiabatic processes.

10 For decades, it has been generally accepted that increased anthropogenic emissions of
11 greenhouse gases are responsible for warming of the lower atmosphere (e.g. Manabe and
12 Wetherald, 1975), and that these emissions are causing the mesosphere and thermosphere to
13 cool (Akmaev and Fomichev, 2000; Roble and Dickinson, 1989). Akmaev and Fomichev
14 (1998) report, using a middle atmospheric model, that if CO₂ concentrations are doubled,
15 temperatures will decrease by about 14 K at the stratopause, by about 10 K in the upper
16 mesosphere and by 40-50 K in the thermosphere. Newer and more sophisticated models
17 include important radiative and dynamical processes as well as interactive chemistries. Some
18 model results indicate a cooling rate near the mesopause less than predicted by Akmaev and
19 Fomichev (1998), while others maintain the negative signal (French and Klekociuk, 2011;
20 Beig, 2011). The thermal response in this region is strongly influenced by changes in
21 dynamics, and some dynamical processes contribute to a warming which counteracts the
22 cooling expected from greenhouse gas emissions (Schmidt et al., 2006).

23 Even though the increasing concentration of greenhouse gases is generally accepted to be the
24 main driver, also other drivers of long-term changes and temperature trends exist, namely
25 stratospheric ozone depletion, long-term changes of solar and geomagnetic activity, secular
26 changes of the Earth's magnetic field, long-term changes of atmospheric circulation and
27 mesospheric water vapour concentration (Laštovička et al., 2012). Dynamics may influence
28 temperatures in the MLT region on time scales of days to months, and investigations of the
29 influence of this variability on averages used for temperature trend assessments are important.
30 The complexity of temperature trends in the MLT region and their causes act as motivation
31 for studying these matters further.

1 In this paper, we investigate trend and variability of temperatures obtained from the NTMR
2 radar, and we also look at summer and winter seasons separately. In Sect. 2, specifications of
3 the NTMR radar are given, and the theory behind the retrieval of temperatures using
4 ambipolar diffusion coefficients from meteor trail echoes is explained. In Sect. 3, the method
5 behind the calibration of NTMR temperatures against Aura MLS temperatures is explained.
6 Section 4 treats trend analysis and analysis of variability and long-period oscillations in
7 temperatures. The theory and underlying assumptions for the method used for determining
8 neutral temperatures from meteor trail echoes and thus how well suited a meteor radar is for
9 estimating such temperatures is discussed in Sect. 5. Also, physical explanations behind
10 change in temperature and observed temperature variability are discussed, as well as
11 comparison with other reports on trends.

12 **2 Instrumentation and data**

13 The Nippon/Tromsø Meteor Radar (NTMR) is located at Ramfjordmoen near Tromsø, at
14 69.58°N, 19.22°E. It is operated 24 hours a day, all year round. Measurements are available
15 for more than 90 % of all days since the radar was first operative in November 2003. The
16 meteor radar consists of one transmitter antenna and five receivers and is operating at 30.25
17 MHz. It detects echoes from ionized trails from meteors, which appear when meteors enter
18 and interact with the Earth's neutral atmosphere in the MLT region. The ionized atoms from
19 the meteors are thermalized, and the resulting trails expand in the radial direction mainly due
20 to ambipolar diffusion, which is diffusion in plasma due to interaction with the electric field.
21 Underdense meteors, which are the ones used in this study, have a plasma frequency that is
22 lower than the frequency of the radar, which makes it possible for the radio wave from the
23 radar to penetrate into the meteor trail and be scattered by each electron.

24 Echoes are detected from a region within a radius of approximately 100 km (horizontal
25 space). The radar typically detects around 10000 echoes a day, of which around 200-600
26 echoes are detected per hour at the peak occurrence height of 90 km. Figure 1 shows the
27 vertical distribution of meteor echoes as a function of height, averaged over the time period
28 2003-2014. The number of echoes detected per day allows for a 30 minute resolution of
29 temperature values. The intra-day periodicity in meteor detections by the NTMR radar is less
30 pronounced than that of lower latitude stations and we do not anticipate tidally-induced bias
31 regarding echo rates at specific tidal phases for daily averages. The height resolution and the

1 range resolution are both 1 km, when looking at altitudes around the peak occurrence height.
2 From the decay time of the radar signal we can derive ambipolar diffusion coefficients, D_a :

$$3 \quad D_a = \frac{\lambda^2}{16\pi^2\tau} \quad (1)$$

4 where λ is the radar wavelength and τ is the radar echo decay time. It has been shown that this
5 coefficient also can be expressed in terms of atmospheric temperature and pressure:

$$6 \quad D_a = 6.39 \times 10^{-2} K_0 \frac{T^2}{p} \quad (2)$$

7 where p is pressure, T is temperature, and K_0 is the zero-field reduced mobility factor of the
8 ions in the trail. In this study we used the value for K_0 of $2.4 \times 10^{-4} \text{ m}^2 \text{ s}^{-1} \text{ V}^{-1}$, in accordance
9 with e.g. Holdsworth et al. (2006). Pressure values were derived from atmospheric densities
10 obtained from falling sphere measurements appropriate for 70°N, combining those of Lübken
11 and von Zahn (1991) and Lübken (1999), previously used by e.g. Holdsworth (2006) and
12 Dyrland et al. (2010). These densities do not take into account long-term solar cycle
13 variations.

14 The NTMR radar is essentially identical to the Nippon/Norway Svalbard Meteor Radar
15 (NSMR) located in Adventdalen on Spitsbergen at 78.33°N, 16.00°E. Further explanation of
16 the radar and explanation of theories can be found in e.g. Hall et al. (2002; 2012), Cervera and
17 Reid (2000) and McKinley (1961).

18 Calibration of temperatures derived from meteor echoes with an independent, coinciding
19 temperature series is necessary, according to previous studies (e.g. Hocking, 1999).
20 Temperatures from the NSMR radar have been derived most recently by Dyrland et al.
21 (2010), employing a new calibration approach for the meteor radar temperatures, wherein
22 temperature measurements from the Microwave Limb Sounder (MLS) on the Aura satellite
23 were used instead of the previously used rotational hydroxyl and potassium lidar temperatures
24 from ground-based optical instruments (Hall et al., 2006). Neither ground-based optical
25 observations nor lidar soundings are available for the time period of interest or the location of
26 the NTMR. In this study we therefore employ the same approach as Dyrland et al. (2010),
27 using Aura MLS temperatures to calibrate the NTMR temperatures.

28 NASA's EOS Aura satellite was launched 15 July 2004 and gives daily global coverage
29 (between 82°S and 82°N) with about 14.5 orbits per day. The MLS instrument is one of four

1 instruments on Aura and samples viewing forward along the spacecraft's flight direction,
2 scanning its view from the ground to ~90 km every ~25 seconds, making measurements of
3 atmospheric temperature, among others (NASA Jet Propulsion Laboratory, 2015).

4 Because of a general cooling of most of the stratosphere and mesosphere the last decades due
5 to e.g. altered concentrations of CO₂ and O₃, the atmosphere has been shrinking, leading to a
6 lowering of pressure surfaces at various altitudes. It is important to distinguish between trends
7 on fixed pressure altitudes and fixed geometric altitudes, since trends on geometric altitudes
8 include the effect of a shrinking atmosphere (Lübken et al., 2013). In this study, we have
9 obtained Aura MLS temperature data (version 3.3) for latitude 69.7°N ± 5.0° and longitude
10 19.0°E ± 10.0° at 90 km geometric altitude.

11 **3 Calibration of NTMR temperatures**

12 Figure 2 shows daily NTMR temperatures from November 2003 to October 2014, derived
13 from Eqs. (1) and (2), plotted together with Aura MLS temperatures. Standard error of the
14 mean is omitted in the plot for better legibility, but typical standard error for daily
15 temperatures is 0.2 - 0.6 K, highest in winter. The Aura satellite overpasses Tromsø at 01-03
16 UTC and 10-12 UTC, which means that the Aura daily averages are representative for these
17 time windows. It was therefore necessary to investigate any bias arising from Aura not
18 measuring throughout the whole day. A way to do this is to assume that Aura temperatures
19 and NTMR temperatures follow the same diurnal variation and thus investigate the diurnal
20 variation of NTMR temperatures. This was done by superposing all NTMR temperatures by
21 time of day, obtaining 48 values for each day, since the radar allows for a 30-minute
22 resolution.

23 There is an ongoing investigation into the possibility that D_a derived by NTMR can be
24 affected by modified electron mobility during auroral particle precipitation. According to
25 Rees et al. (1972), neutral temperatures in the auroral zone show a positive correlation with
26 geomagnetic activity. It is therefore a possibility that apparent D_a enhancements during strong
27 auroral events do not necessarily depict neutral temperature increase. This matter requires
28 further attention.

29 Plotting hourly D_a values shows clear evening enhancements, especially during winter (not
30 shown here). Investigation of possible unrealistic D_a enhancements was carried out by
31 calculating standard errors of estimated hourly D_a values:

$$1 \quad se = \frac{\sigma}{\sqrt{ne}} \quad (3)$$

2 where σ is standard deviation and ne is the number of echoes detected by the radar. By
 3 examining and testing different rejection criteria, we arrived at a threshold of 7 % in standard
 4 error of hourly D_a values for identifying unrealistic enhancements. This rejection criterion led
 5 to that 5.4 % of the D_a values were rejected. NTMR temperatures after application of the D_a
 6 rejection procedure will hereafter be referred to as D_a -rejected NTMR temperatures.

7 Figure 3 shows monthly averages of the superposed values of D_a -rejected NTMR
 8 temperatures as a function of time of day for days coinciding with Aura measurements. It is
 9 evident from the figure that the lowest temperatures are in general achieved in the forenoon,
 10 which coincides with one of the periods per day when Aura MLS makes measurements over
 11 Tromsø.

12 Subtracting monthly averages of the 00-24 UTC temperatures from the 01-03 UTC and 10-12
 13 UTC temperatures gave the estimated biases in Aura daily means due to only sampling during
 14 some hours of the day and are given in Table 1. By judging by the measurement windows,
 15 Aura underestimates the daily mean (00-24 UTC) more during winter than during spring and
 16 summer. Note the higher standard deviations in spring and summer compared to winter.

17 The initially obtained Aura temperatures were corrected by adding the biases from Table 1 in
 18 order to arrive at daily mean temperatures that were representative for the entire day. Also, the
 19 Aura temperatures were corrected for “cold bias”. French and Mulligan (2010) report that
 20 Aura MLS temperatures exhibit a 10 K cold bias compared with OH*(6-2) nightly
 21 temperatures at Davis Station, Antarctica. A newer study by Garcia-Comas et al. (2014)
 22 shows that Aura MLS exhibits a bias compared with several satellite instruments which varies
 23 with season. According to their findings, a 10 K correction for cold bias was applied to the
 24 Aura summer and winter temperatures (Jun – Aug, Dec - Feb), while a 5 K correction was
 25 applied to autumn and spring temperatures (Sep – Nov, Mar – May). The corrected Aura
 26 temperatures will hereafter be referred to as local time and cold bias-corrected Aura MLS
 27 temperatures.

28 Local time and cold bias-corrected Aura temperatures were plotted against D_a -rejected NTMR
 29 temperatures, and the linear fit ($R^2 = 0.83$) is described by:

$$30 \quad T_{NTMR} = 0.84T_{Aura} + 32 \quad (4)$$

1 where T_{NTMR} is D_a -rejected temperature obtained from NTMR, and T_{Aura} is local time and cold
2 bias-corrected temperature from Aura MLS. Inverting Eq. (4) enabled us to estimate NTMR
3 temperatures calibrated with respect to Aura MLS temperatures. NTMR temperatures were
4 now corrected for days of measurements coinciding with Aura measurements and are
5 hereafter referred to as MLS-calibrated NTMR temperatures. For calibration of NTMR
6 temperatures from November 2003 to August 2004 (before the beginning of the Aura MLS
7 dataset), D_a -rejected NTMR temperatures were used as input to the inverted equation to arrive
8 at calibrated NTMR temperatures.

9 To estimate the calibration uncertainty, all local time and cold bias-corrected Aura
10 temperatures were subtracted from the MLS-calibrated NTMR temperatures, and the
11 differences were plotted in a histogram with 5 K bins (not shown here). A Gaussian was fitted
12 to the distribution. The standard deviation of the Gaussian was 11.9 K, which is considered
13 the overall uncertainty of the calibration. Finally, Fig. 4 shows the MLS-calibrated NTMR
14 temperatures with uncertainties plotted together with Aura MLS temperatures, corrected for
15 cold and time-of-day measurement bias.

16 **4 Results**

17 Weatherhead et al. (1998) discuss the effects of autocorrelation and variability on trend
18 estimation and emphasize that changes in environmental variables are often modelled as being
19 a linear change, even though there may be a high degree of periodic variation within the data
20 in addition to the linear trend. A linear trend model assumes that measurements of the variable
21 of interest at time t can be expressed as:

$$22 \quad Y_t = \mu + S_t + \omega L_t + N_t \quad (5)$$

23 where μ is a constant term, S_t is a seasonal component, L_t is the linear trend function, ω is the
24 magnitude of the trend and N_t is noise. N_t may be autocorrelated and the result of various
25 natural factors, which give rise to somewhat smoothly varying changes in N_t over time. Such
26 natural factors may not always be known or measurable.

27 Taking this into account, variability of the data was explored before assessing the linear trend
28 of the temperature data. In Sect. 4.1, Lomb-Scargle periodogram analysis is conducted, and
29 periodic components in the data are identified before assessing trend, while in Sect. 4.2 solar
30 cycle dependence is briefly explored, even though the temperature record is too short for this
31 to be incorporated in the trend analysis.

1 4.1 Estimation of periodic variability and trend

2 To identify periodic variability, a Lomb-Scargle (LS) periodogram analysis was applied to the
3 MLS-corrected NTMR temperatures (Press and Rybicki, 1989). LS analysis is a modified
4 discrete Fourier transform algorithm suitable for unevenly spaced data. Figure 5 (upper panel)
5 shows the LS periodogram, identifying a particularly strong annual (A) component, but also a
6 semi-annual (A/2) and two sub-annual peaks (A/3 and A/4), significant at the 99 % level.

7 Following the procedure of Niciejewski and Killeen (1995), the daily temperatures were fit to
8 the approximation

$$9 \quad T_{NTMR}(t) = T_0 + \sum_i \left(d_i \sin \frac{2\pi}{p_i} t + e_i \cos \frac{2\pi}{p_i} t \right) + Lt \quad (6)$$

10 where $T_{NTMR}(t)$ is observed daily temperature, T_0 is the average temperature, i is the number of
11 harmonic components found in the LS analysis, d_i and e_i are the amplitudes of the i^{th}
12 harmonic component, p_i is the period of the i^{th} harmonic component and t is the day number. L
13 represents the trend. The average temperature over the 11 year period, T_0 , was found to be
14 189.4 ± 0.6 K.

15 It has been shown that the confidence levels in the periodogram are only strictly valid for the
16 peak with the highest spectral power (Scargle, 1982). Thus, there may be peaks significant at
17 the 95 % level even though they are not noticeable in the periodogram, due to that their
18 variance is overestimated by the presence of the larger peaks. Therefore, after fitting the
19 primary periodic components with significance better than the 99 % level to the NTMR
20 temperatures using Eq. (6), LS analysis was repeated on the temperature residuals to check for
21 additional significant periodic components in the data. Horne and Baliunas (1986) pointed out
22 that the periodogram power needs to be normalized by the total variance of the data in order
23 to obtain spectral peaks with correct magnitude. The variance of the data was therefore
24 adjusted to maintain the correct probability distribution of the periodogram. Figure 5 (lower
25 panel) shows spectral power of harmonics found at better than 95 % significance level of
26 residuals obtained after fitting the sinusoids of the four largest peaks. The apparently
27 significant peaks located near 91, 121, 184 and 363 days, even though these harmonics have
28 been filtered out at this stage, are due to spectral leakage, which means that for a sinusoidal
29 signal at a given frequency, ω_0 , the power in the periodogram not only appears at ω_0 , but also

1 leaks to other nearby frequencies (Scargle, 1982). All periodic components found at better
2 than 95 % significance and their amplitudes are listed in Table 2.

3 The trend was estimated from the approximation in Eq. (6) to be $-2.2 \text{ K} \pm 1.0 \text{ K/decade}$. From
4 Tiao et al. (1990), this trend can be considered significantly non-zero at the 5 % level, since
5 the uncertainty ($2\sigma = 2.0 \text{ K/decade}$) is less than the trend itself. We estimated the number of
6 years for which a trend can be detectable, following the formulation of Weatherhead et al.
7 (1998):

$$8 \quad n^* \approx \left[\frac{3.3\sigma_N}{|\omega_0|} \sqrt{\frac{1+\varphi}{1-\varphi}} \right]^{2/3} \quad (7)$$

9 where n^* is the number of years required, ω_0 is the magnitude of the trend per year, σ_N is the
10 standard deviation of noise N and φ is the autocorrelation function of the noise at lag 1. The
11 value 3.3 corresponds to a 90 % probability that the trend is detectable after n^* years. Solving
12 Eq. (7) reveals that the minimum number of years required for detecting a decadal trend of -
13 2.2 K is about 17 years.

14 The resulting composite of the least-squares fit is shown in Fig. 6, together with the MLS-
15 corrected NTMR temperatures. We see that the smooth curve represents the periodicity in the
16 data to a good extent, but there is still variability not accounted for. Temperature residuals
17 obtained after subtracting the MLS-calibrated NTMR temperatures from the fit in Fig. 6 are
18 henceforth referred to as fit residuals.

19 In addition to the harmonics listed in Table 2, we found a harmonic of ~ 615 days (see Fig. 5,
20 lower panel), not statistically significant. We also found a ~ 17 day oscillation, significant at
21 the 95 % level (see Fig. 5, lower panel), but the amplitude of this component was found to be
22 close to 0 K. The 615 day and 17 day periodic components were therefore not incorporated in
23 the composite fit.

24 In Fig. 7, all individual years are superposed by day-of-year. This was done to better visualize
25 the variability of an average year. In addition to the broad maximum in temperatures during
26 winter and the narrower minimum during summer, we see minor enhancements just after
27 spring equinox (day-of-year ~ 100) and summer solstice (day-of-year ~ 210), and also a local
28 minimum in early winter. Explanations for the variability will be discussed in Sect. 5.1.

1 In addition to the average temperature change, we also treated summer and winter seasons
2 separately. First, monthly averages of the temperature residuals were calculated and trends for
3 each month were investigated. Figure 8 shows the result. Then, averages of November,
4 December and January, and of May, June and July were made. As opposed to the
5 “meteorological” seasons as experienced in the troposphere, we have chosen to define
6 “winter” and “summer” as the three months centred on the respective solstices. However,
7 since the meteorological winter and summer are defined differently, we will refer to these
8 trends as NDJ and MJJ trends, The linear NDJ trend is $-11.6 \text{ K} \pm 4.1 \text{ K/decade}$, and the MJJ
9 trend is $-0.3 \text{ K} \pm 3.1 \text{ K/decade}$. Solving Eq. (7) for NDJ and MJJ trends reveals a minimum
10 length for trend detection of 10.8 years and 63 years, respectively.

11 The trend analysis was also performed without carrying out the D_a rejection procedure
12 explained in Sect. 3. Final results of the trend analysis, both when excluding and including
13 rejection of D_a values due to hypothetical anomalous electrodynamic processes, do not differ
14 significantly. It is reasonable to believe that strong geomagnetic conditions can affect derived
15 temperatures on a short time scale. However, due to the considerable quantity of data
16 employed in this study, it is inconceivable that this effect will change the conclusions
17 regarding trends, as our results also show.

18 **4.2 Exploration of solar flux dependence**

19 Our dataset covers 11 years of meteor radar temperatures and thus it is shorter than the
20 corresponding solar cycle (which was somewhat longer than the average 11 years). Even
21 though it is premature to apply solar cycle analysis to a time series this short, we will briefly
22 explore and present our temperature data together with solar variability. In this study we use
23 the F10.7 cm flux as a proxy for solar activity, which is the most commonly used index in
24 middle/upper atmospheric temperature trend studies (e.g. Laštovička et al., 2008; Hall et al.,
25 2012).

26 Figure 9 shows yearly values of F10.7 cm plotted against yearly averaged fit residual
27 temperatures. For clarity, black bullets corresponding to years are connected with lines,
28 making it easier to see the progression from high solar flux to solar minimum and back to
29 solar maximum. We see that, to some extent, there is a conjunction between low solar flux
30 values and negative temperature fit residuals. For years 2006 – 2010, which were years of
31 solar minimum, fit residuals were on average negative. For years 2005 and 2011, which were

1 years in between solar maximum and minimum, fit residuals were close to zero. However, for
2 years with higher F10.7 values the tendency of increasing fit residuals is less distinct. Ogawa
3 et al. (2014) find a non-linear relationship between upper atmospheric temperatures and solar
4 activity using EISCAT UHF radar observations from 200 to 450 km altitude over Tromsø,
5 even though it must be noted that the altitude range they look at differs from ours.

6 **5 Discussion**

7 Statistical significant periodic components found in the temperature data are annual (A) and
8 semi-annual (A/2) oscillations, and 121 (A/3), 91 (A/4), 69 (A/5), 52 (A/7), 46 (A/8), 32 and
9 9 day oscillations. Temperature change from 2003 to 2014 is $-2.2 \text{ K} \pm 1.0 \text{ K/decade}$, and MJJ
10 and NDJ trends are $-0.3 \text{ K} \pm 3.1 \text{ K/decade}$ and $-11.6 \text{ K} \pm 4.1 \text{ K/decade}$, respectively.
11 Explanations for the periodic variability will be proposed in Sect. 5.1. In Sect. 5.2, physical
12 explanations for the temperature change will be explored, and our results will be compared to
13 other reports on mesospheric trends at high and mid-latitudes. Trends will be discussed in
14 terms of the method used for deriving temperatures in Sect. 5.3.

15 **5.1 Mechanisms for the observed variability and harmonics**

16 The A, A/2, A/3, A/4, A/5, A/7 and A/8 components are also found for OH* temperatures
17 over other mid and high-latitude sites (e.g. Espy and Stegman, 2002; Bittner et al., 2000;
18 French and Burns, 2004). In addition to these components, A/6 and A/9 sub-annual
19 harmonics, as well as other shorter-period components, have been identified in other datasets
20 (e.g. Bittner et al., 2000; French and Burns, 2004).

21 Espy and Stegman (2002) attribute the asymmetry with the broad winter maximum and the
22 narrow summer minimum to the A/2 harmonic, and the temperature enhancements during
23 equinoxes to the A/3 and A/4 harmonics.

24 French and Burns (2004) identify the visible variations of the 52-day (A/7) component in their
25 data from Davis, Antarctica, and find this component's phase to be "locked" to the day-of-
26 year, indicating a seasonal dependence. Espy and Stegman (2002) only find this component as
27 a result of LS analysis of their superposed-epoch data, also indicating that the phase is locked
28 to day-of-year. French and Burns (2002) and Bittner et al. (2000) find in general strong
29 differences from year to year in the significant oscillations observed. We have not carried out
30 analysis of the year-to-year variation in oscillations observed, but considering e.g. the uneven
31 occurrences of SSWs we have no reason to conclude otherwise regarding our data.

1 The ~9 day oscillation we find in our data can most likely be designated to travelling
2 planetary waves, which have typical periods of 1-3 weeks, with 8-10 days as a prominent
3 period (Salby 1981a,b).

4 The ~615 day periodic component (not statistically significant) may at first glance seem to be
5 somehow related to the quasi-biennial oscillation (QBO), which is a system where zonal
6 winds in the lower equatorial stratosphere alternate between westward (easterly) and eastward
7 (westerly) with a mean period of 28-29 months. Also other studies find a ~2 year periodic
8 component in their temperature data, attributed to a QBO effect (Espy and Stegman, 2002;
9 Bittner et al., 2000; French and Burns, 2004 – the two latter give statistically inconclusive
10 results). However, our ~615 day component is quite far from the mean period of the QBO.
11 That, in addition to that it is not significant, makes it difficult to interpret.

12 The higher temperature variability during winter compared to summer, visible in Fig. 7, is
13 also found in other datasets at mid and high-latitudes (e.g. Espy and Stegman, 2002; Bittner et
14 al., 2000). This feature and the observations of local temperature enhancement around day
15 200 and the reduction of the strong, negative seasonal gradient just after spring equinox can
16 be explained by the state of the background wind system in the middle atmosphere and the
17 corresponding propagation of planetary and gravity waves. Enhanced GW and PW flux and
18 momentum into the mesosphere lead to enhanced turbulent diffusion which can result in
19 increased temperatures. PWs can only propagate westward and against the zonal flow, so
20 easterly winds in the middle atmosphere during summer are blocking vertical propagation of
21 long-period PWs into the MLT region. In contrast, during winter stratospheric zonal winds
22 are westerly, favouring PW propagation. The presence of upward-propagating PWs during
23 winter is therefore an explanation for the higher variability during this season.

24 GWs can propagate both eastward and westward, but only against the zonal flow, implying
25 the presence of eastward-propagating GWs during summer and westward-propagating GWs
26 during winter. The extratropical meso-stratospheric zonal winds are very weak and change
27 direction during the equinoxes, resulting in a damping of both westward- and eastward-
28 propagating GWs during these periods (Hoffmann et al., 2010). Enhanced PW activity is
29 observed at the same time (Stray et al., 2014). Temperature enhancements after spring
30 equinox are related to the final breakdown of the polar vortex, or the last stratospheric
31 warming event (Shepherd et al., 2002). Several studies have observed a “springtime tongue”
32 of westward flow between 85 and 100 km, occurring approximately from day 95 to 120,

1 reflecting the final warming (e.g. Hoffmann et al., 2010; Manson et al., 2002). The final
2 warming is characterised by forced planetary Rossby waves that exert a strong westward
3 wave drag from the stratosphere up to 100 km.

4 Enhanced PW activity has also been observed during midsummer, due to interhemispheric
5 propagation of PWs into the summer mesopause (Stray et al., 2014, Hibbins et al., 2009).
6 Also, enhanced short-period GW activity has been observed during summer (Hoffmann et al.,
7 2010). Increased temperatures during midsummer may thus be a result of the combined effect
8 of upward-propagating GWs and interhemispheric propagation of PWs.

9 Several studies have identified large temperature amplitude perturbations during the autumn
10 equinox in particular (Taylor et al. 2001; Liu et al., 2001). The same signature is hard to find
11 in our data. Hoffmann et al. (2010) find latitudinal differences in the amplitude of the
12 semidiurnal meridional tide during autumn equinox, observing stronger tidal amplitudes at
13 Juliusruh (55°N, 13°E) compared to Andenes (69°N, 16°E). Manson et al. (2009) also find
14 longitudinal differences in tides at high-latitudes. Reasons for not observing increased
15 temperatures around autumn equinox are not clear, and further investigations are needed in
16 order to conclude on this.

17 The local temperature minimum in early winter is also seen in other temperature data from
18 mid and high-latitudes (e.g. French and Burns, 2004; Holmen et al., 2013; Shepherd et al.,
19 2004). French and Burns (2004) find a decrease in large-scale wave activity during midwinter
20 which they associate with the observed temperature minimum, but identify this as a southern
21 hemisphere phenomenon. Shepherd et al. (2004) attribute the decrease in temperature to early
22 winter warming of the stratosphere, characterized by the growth of upward-propagating PWs
23 from the troposphere which decelerate/reverses the eastward stratospheric jet, resulting in
24 adiabatic heating of the stratosphere and adiabatic cooling of the mesosphere. However,
25 Shepherd et al. used temperature data from 1991 to 1999, which is prior to the start of our
26 temperature record, and timings of SSWs are different from year to year. We investigated the
27 timing and occurrence of SSW events during the last decade using NASA reanalysis
28 temperatures and zonal winds provided through the Modern-Era Retrospective analysis for
29 Research and Applications (MERRA) project (NASA, 2016). Most SSWs occurring between
30 2003 and 2014 start in the beginning of January or mid-January. One exception is the major
31 warming in 2003/2004, in which zonal winds started to decelerate in mid-December. There
32 are signs of a minor warming in the transition between November and December 2012, but

1 there is not enough evidence to conclude that the local minimum of NTMR temperatures
2 starting in early November is associated with early winter warming of the stratosphere. It is
3 more likely that the pronounced variability in temperatures we see in January and February
4 (days ~0-50) in Fig. 7 is a manifestation of the SSW effect.

5 **5.2 Physical explanations for cooling and comparison with other studies**

6 Other studies on long-term mesospheric temperature trends from mid and high-latitudes yield
7 mostly negative or near-zero trends. Few studies cover the same time period as ours, and few
8 are from locations close to Tromsø. Hall et al. (2012) report a negative trend of $-4 \text{ K} \pm 2$
9 K/decade for temperatures derived from the meteor radar over Longyearbyen, Svalbard
10 (78°N , 16°E) at 90 km height over the time period 2001 to 2011, while Holmen et al. (2014)
11 find a near-zero trend for OH* airglow temperatures at ~87 km height over Longyearbyen
12 over the longer time period 1983 to 2013. Offermann et al. (2010) report a trend of $-2.3 \text{ K} \pm$
13 0.6 K/decade for ~87 km height using OH* airglow measurements from Wuppertal (51°N ,
14 7°E). It must be noted that the peak altitude of the OH* airglow layer can vary and thus affect
15 the comparability of OH* airglow temperature trends and meteor radar temperature trends.
16 Winick et al., 2009 report that the OH* airglow layer can range from 75 to >90 km, while the
17 newer study by von Savigny, 2015, indicates that the layer height at high-latitudes is
18 remarkably constant from 2003 to 2011. Beig (2011) report that most recent studies on
19 mesopause region temperature trends show weak negative trends, which is in line with our
20 results.

21 According to the formulation by Weatherhead et al. (1998), our time series is not long enough
22 for significant trend detection. We need another ~6 years of data before a trend of magnitude -
23 $2.2 \text{ K} \pm 1.0 \text{ K/decade}$ is significant. Response to solar variability has not been taken into
24 account due to the length of the temperature record. Our slightly negative overall trend must
25 therefore be considered tentative. The summer trend requires many more years of data before
26 it can be considered significant, due to that it is a near-zero trend. However, the winter trend
27 can be considered detectable and also significantly different from zero, following the criteria
28 from Weatherhead et al. (1998) and Tiao et al. (1990).

29 Our results indicate a cooling at 90 km altitude over Tromsø in winter. A general cooling of
30 the middle atmosphere will cause a contraction of the atmospheric column and hence a
31 lowering of upper mesospheric pressure surfaces. The pressure model used as input to Eq. (2)

1 is only seasonally dependent, so a possible trend in pressure at 90 km must be addressed. By
2 looking at Eq. (2), it is evident that if pressure decreases, temperature will decrease even
3 more. Incorporating a decreasing trend in the pressure model will then serve to further
4 strengthen the negative temperature trend we observe.

5 It has been proposed that GWs may be a major cause of negative temperature trends in the
6 mesosphere and thermosphere (Beig, 2011; Oliver et al., 2013). GWs effectively transport
7 chemical species and heat in the region, and increased GW drag leads to a net effect of
8 cooling above the turbopause (Yigit and Medvedev, 2009). GWs are shown to heat the
9 atmosphere below about 110 km altitude, while they cool the atmosphere at higher altitudes
10 by inducing a downward heat flux (Walterscheid, 1981). However, there are large regional
11 differences regarding trends in GW activity. Hoffmann et al. (2011) find an increasing GW
12 activity in the mesosphere in summer for selected locations, but Jacobi (2014) finds larger
13 GW amplitudes during solar maximum and relates this to a stronger mesospheric jet during
14 solar maximum, both for winter and summer. Since we have not conducted any gravity wave
15 trend assessment in this study, we cannot conclude that GW activity is responsible for the
16 negative temperature trend, but we cannot rule out its role either.

17 The stronger cooling trend for winter is also consistent with model studies. Schmidt et al.
18 (2006) and Fomichev et al. (2007) show, using the HAMMONIA and CMAM models,
19 respectively, that a doubling of the CO₂ concentration will lead to a general cooling of the
20 middle atmosphere, but that the high-latitude summer mesopause will experience insignificant
21 change or even slight warming. They propose that this is the result of both radiative and
22 dynamical effects. In summer, the CO₂ radiative forcing is positive due to heat exchange
23 between the cold polar mesopause and the warmer, underlying layers. Also, CO₂ doubling
24 alters the mesospheric residual circulation. This change is caused by a warming in the tropical
25 troposphere and cooling in the extratropical tropopause, leading to a stronger equator-to-pole
26 temperature gradient and hence stronger mid-latitude tropospheric westerlies. This causes the
27 westerly gravity wave drag to weaken, resulting in decreased adiabatic cooling from a slower
28 ascent of the upper mesospheric circulation. However, it must be noted that our strong,
29 negative NDJ trend may differ from a trend estimated for meteorological winter months.

5.3 Suitability of a meteor radar for estimation of neutral temperatures at 90 km height

As explained in Sect. 2, neutral air temperatures derived from meteor trail echoes depend on pressure, p , the zero-field reduced mobility of the ions in the trail, K_0 , and ambipolar diffusion coefficients, D_a . K_0 will depend on the ion composition in the meteor trail, as well as the chemical composition of the atmosphere. The chemical composition of the atmosphere is assumed to not change significantly with season (Hocking, 2004). Unfortunately, the exact content of a meteor trail is unknown. Usually, a value for K_0 between $1.9 \cdot 10^{-4} \text{ m}^2 \text{ s}^{-1} \text{ V}^{-1}$ and $2.9 \cdot 10^{-4} \text{ m}^2 \text{ s}^{-1} \text{ V}^{-1}$ is chosen, depending on what ion one assumes to be the main ion of the trail (Hocking et al., 1997). Even though we in this study have chosen a constant value for K_0 of $2.4 \cdot 10^{-4} \text{ m}^2 \text{ s}^{-1} \text{ V}^{-1}$, some variability in K_0 is expected. According to Hocking (2004) variability can occur due to fragmentation of the incoming meteoroid, anisotropy in the diffusion rate, plasma instabilities and variations in the composition of the meteor trail. Using computer simulations, they report a typical variability in K_0 from meteor to meteor of 27 % and that the variability is most dominant at higher temperatures. Based on this, we cannot rule out sources of error due to the choice of K_0 as a constant, but since we have no possibility to analyse the composition of all meteor trails detected by the radar we have no other choice than to choose a constant value for K_0 .

How well ambipolar diffusion coefficients obtained for 90 km altitude are suited for calculating neutral temperatures has previously been widely discussed, e.g. by Hall et al. (2012) for the trend analysis of Svalbard meteor radar data, but will be shortly repeated here. For calculations of temperatures using meteor radar, ambipolar diffusion alone is assumed to determine the decay of the underdense echoes. Diffusivities are expected to increase exponentially with height through the region from which meteor echoes are obtained (Ballinger et al., 2008; Chilson et al., 1996). Hall et al. (2005) find that this is only the case between ~85 and ~95 km altitude, using diffusion coefficients delivered by NTMR from 2004. They find diffusivities less than expected above ~95 km and diffusivities higher than expected below ~85 km. Ballinger et al. (2008) obtain a similar result using meteor observations over northern Sweden. It has been proposed that processes other than ambipolar diffusion influence meteor decay times. If this is the case it may have consequences for the estimation of temperatures, and therefore it is important to investigate this further.

1 Departures of the anticipated exponential increase with height of molecular diffusion above
2 ~95 km are in previous studies attributed to gradient-drift Farley-Buneman instability. Farley-
3 Buneman instability occurs where the trail density gradient and electric field are largest. Due
4 to frequent collisions with neutral particles, electrons are magnetised while ions are left
5 unmagnetised, causing electrons and ions to differ in velocity. Electrons then create an
6 electric field perpendicular to the meteor trail, leading to anomalous fading times that can be
7 an order of magnitude higher than those expected from ambipolar diffusion. The minimum
8 altitude at which this occurs depends on the trail altitude, density gradient and latitude, and at
9 high-latitudes this altitude is ~95 km. Therefore, using ambipolar diffusion rates to calculate
10 trail altitudes above this minimum altitude may lead to errors of several kilometres, due to
11 that the diffusion coefficients derived from the measurements are underestimated (Ballinger et
12 al., 2008; Dyrud et al., 2001; Kovalev et al., 2008).

13 Reasons for the higher diffusivities than expected according to theory below ~85 km are not
14 completely understood. Hall (2002) proposes that neutral turbulence may be responsible for
15 overestimates of molecular diffusivity in the region ~70-85 km, but this hypothesis is rejected
16 by Hall et al. (2005) due to a lacking correlation between neutral air turbulent intensity and
17 diffusion coefficients delivered by the NTMR radar. Other mechanisms for overestimates of
18 molecular diffusivity include incorrect determination of echo altitude and fading times due to
19 limitations of the radar (Hall et al., 2005).

20 Since the peak echo occurrence height is 90 km and this is also the height at which a
21 minimum of disturbing effects occur, 90 km height is therefore considered the optimal height
22 for temperature measurements using meteor radar. Ballinger et al. (2008) report that meteor
23 radars in general deliver reliable daily temperature estimates near the mesopause using the
24 method outlined in this study, but emphasize that one should exercise caution when assuming
25 that observed meteor echo fading times are primarily governed by ambipolar diffusion. They
26 propose, after Havnes and Sigernes (2005), that electron-ion recombination can impact
27 meteor echo decay times. Especially can this affect the weaker echoes, and hence can this
28 effect lead to underestimation of temperatures.

29 Determination of temperatures from meteor radar echo times is a non-trivial task, mainly
30 because the calculation of ambipolar diffusion coefficients depends on the ambient
31 atmospheric pressure. By using radar echo decay times to calculate ambipolar diffusion
32 coefficients from Eq. (1), we can from Eq. (2) get an estimate for T^2/p . Input of pressure

1 values into the equation will thus provide atmospheric temperatures. However, measurements
2 of pressure are rare and difficult to achieve at 90 km height, and often one has to rely on
3 model values. Traditionally, pressure values at 90 km have been calculated using the ideal gas
4 law, taking total mass density from atmospheric models, e.g. the MSISE models, where the
5 newest version is NRLMSIS-00. It is hard to verify the pressure values derived from the
6 models because of lack of measurements to compare the model to, and hence using the
7 pressure values may result in uncertainties of estimated atmospheric temperatures. In this
8 study, we obtained pressure values from measurements of mass densities obtained from
9 falling spheres combined with sodium lidar from Andøya (69°N, 15.5°E) (Lübken, 1999;
10 Lübken and von Zahn, 1991). All measurements have been combined to give a yearly
11 climatology, that is, one pressure value for each day of the year. Since Andøya is located in
12 close proximity to Tromsø (approximately 120 km), the pressure values are considered
13 appropriate for our calculations of neutral temperatures. One disadvantage with using pressure
14 values obtained from the falling sphere measurements is that no day-to-day variations are
15 taken into account, only the average climatology.

16 **6 Conclusions**

17 A number of long-period oscillations ranging from ~9 days to a year were found in the
18 NTMR temperature data. Temperature variability observed may, to a large extent, be
19 explained by the large-scale circulation of the middle atmosphere and the corresponding
20 activity in waves propagating from below. Higher temperature variability in winter is due to
21 the presence of upward-propagating PWs during this season, in contrast to summer, when
22 easterly winds in the middle atmosphere are blocking vertical propagation of long-period PWs
23 into the MLT region. The variability is particularly high in January and February, which are
24 periods where SSW events occur frequently. In addition to the general maximum of
25 temperatures in winter and minimum in summer, our data shows a local temperature
26 enhancement around day 210, a local minimum in early winter and reduction of the strong,
27 negative seasonal gradient after spring equinox. The reduction of the strong, negative seasonal
28 gradient after spring equinox is related to the final breakdown of the polar vortex (Shepherd et
29 al., 2002), while the increase during summer most likely is associated with a combined effect
30 of upward-propagating GWs and interhemispheric propagation of PWs (Stray et al., 2014;
31 Hoffmann et al., 2010). No evident reason can be found for the local temperature minimum in

1 early winter, or the fact that we do not see enhanced temperatures during autumn equinox, as
2 identified by others (e.g. Taylor et al., 2001; Liu et al., 2001).

3 The trend for NTMR temperatures at 90 km height over Tromsø was found to be $-2.2 \text{ K} \pm 1.0$
4 K/decade . Summer (May, June, July) and winter (November, December, January) trends are -
5 $0.3 \text{ K} \pm 3.1 \text{ K/decade}$ and $-11.6 \text{ K} \pm 4.1 \text{ K/decade}$, respectively. Following the criterion from
6 Weatherhead et al. (1998), the temperature record is only long enough for the NDJ trend to be
7 considered detectable. Response to solar variability was not incorporated in the trend, due to
8 that the time series is shorter than the corresponding solar cycle. However, when looking at
9 the progression from high solar flux to solar minimum and back to solar maximum we see, to
10 some extent, that there is a conjunction between low solar flux values and negative
11 temperature fit residuals and vice versa.

12 A weak overall cooling trend is in line with other recent studies on mesopause region
13 temperature trends. A cooling of the middle atmosphere will cause a lowering of upper
14 mesospheric pressure surfaces. By implementing a negative trend in pressure at 90 km into
15 the equation we use for estimating temperatures the negative temperature trend is enhanced,
16 which reinforces our finding of a cooling trend. The most accepted theory behind a cooling of
17 the middle atmosphere is increased greenhouse gas emissions, which may lead to a change in
18 dynamics. Our results yield a more negative trend in winter compared to summer, which may
19 be explained by radiative and dynamical effects. In summer, a larger heat exchange takes
20 place from atmospheric layers below the cold, polar mesopause. Weakening of gravity wave
21 drag leads to weakening of the mesospheric residual circulation, which counteracts cooling.
22 These effects occur due to increased CO_2 concentrations in the atmosphere, according to
23 model studies.

24 **Acknowledgements**

25 The research for this article was financially supported by The Research Council of Norway
26 through contract 223252/F50 (CoE). NTMR operation was supported by Research Project
27 KP-9 of National Institute of Polar Research. The authors are grateful to the NASA EOS Aura
28 MLS team for providing free access to the MLS temperature data, and to Frank Mulligan at
29 Maynooth University, Ireland, for providing downloaded data specific for Tromsø. In
30 addition, the authors wish to express their appreciation to the referees of this paper.

1 References

- 2 Akmaev, R. A. and V. I. Fomichev: Cooling of the mesosphere and lower thermosphere due
3 to doubling of CO₂, *Ann. Geophys.*, 16, 1501-1512, doi: 10.1007/s00585-998-1501-z, 1998.
- 4 Akmaev, R. A. and V. I. Fomichev: A model estimate of cooling in the mesosphere and lower
5 thermosphere due to the CO₂ increase over the last 3-4 decades, *Geophys. Res. Lett.*, 27 (14),
6 2113-2116, doi: 10.1029/1999GL011333, 2000.
- 7 Ballinger, A. P., P. B. Chilson, R. D. Palmer, and N. J. Mitchell: On the validity of the
8 ambipolar diffusion assumption in the polar mesopause region, *Ann. Geophys.*, 26, 3439-
9 3443, doi: 10.5194/angeo-26-3439-2008, 2008.
- 10 Beig, G.: Long-term trends in the temperature of the mesosphere/lower thermosphere region:
11 1. Anthropogenic influences, *J. Geophys. Res. – Space Physics*, 116, A00H11, doi:
12 10.1029/2011JA016646, 2011.
- 13 Bittner, M., D. Offermann, and H. H. Graef: Mesopause temperature variability above a
14 midlatitude station in Europe, *J. Geophys. Res.*, 105 (D2), 2045-2058, doi:
15 10.1029/1999JD900307, 2000.
- 16 Cervera, M. A. and I. M. Reid: Comparison of atmospheric parameters derived from meteor
17 observations with CIRA, *Radio Sci.*, 35 (3), 833-843, doi: 10.1029/1999RS002226, 2000.
- 18 Chilson, P. B., P. Czechowsky, and G. Schmidt: A comparison of ambipolar diffusion
19 coefficients in meteor trains using VHF radar and UV lidar, *Geophys. Res. Lett.*, 23 (20),
20 2745-2748, doi: 10.1029/96gl02577, 1996.
- 21 Dyrland, M. E., C. M. Hall, F. J. Mulligan, M. Tsutsumi, and F. Sigernes: Improved estimates
22 for neutral air temperatures at 90 km and 78°N using satellite and meteor radar data, *Radio*
23 *Sci.*, 45 (RS4006), doi: 10.1029/2009rs004344, 2010.
- 24 Dyrud, L. P., M. M. Oppenheim, and A. F. vom Endt: The anomalous diffusion of meteor
25 trails, *Geophys. Res. Lett.*, 28 (14), 2775-2778, doi: 10.1029/2000GL012749, 2001.
- 26 Espy, P. J., and J. Stegman: Trends and variability of mesospheric temperature at high-
27 latitudes, *Phys. Chem. Earth.*, 27, 543-553, doi: 10.1016/S1474-7065(02)00036-0, 2002.
- 28 Fomichev, V. I., A. I. Jonsson, J. de Grandpré, S. R. Beagley, C. McLandress, K. Semeniuk,
29 and T. G. Shepherd: Response of the middle atmosphere to CO₂ doubling: Results from the

1 Canadian Middle Atmosphere Model, *J. Climate*, 20, 1121-1144, doi: 10.1175/JCLI4030.1,
2 2007.

3 Forbes, J. M., Zhang, X., and Marsh, D. R.: Solar cycle dependence of middle atmosphere
4 temperatures, *J. Geophys. Res. Atmos.*, 119, 9615-9625, doi:10.1002/2014JD021484, 2014.

5 French, W. J. R., and G. B. Burns: The influence of large-scale oscillations on long-term trend
6 assessment in hydroxyl temperatures over Davis, Antarctica, *J. Atm. Solar-Terr. Phys.*, 66,
7 493-506, doi: 10.1016/j.jastp.2004.01.027, 2004.

8 French, W. J. R. and A. R. Klekociuk: Long-term trends in Antarctic winter hydroxyl
9 temperatures, *J. Geophys. Res.*, 116, D00P09, doi: 10.1029/2011JD015731, 2011.

10 French, W. J. R. and F. J. Mulligan: Stability of temperatures from TIMED/SABER v1.07
11 (2002-2009) and Aura/MLS v2.2 (2004-2009) compared with OH(6-2) temperatures observed
12 at Davis Station, Antarctica, *Atm. Chem. Phys.*, 10, 11439-11446, doi: 10.5194/acp-10-
13 11439-2010, 2010.

14 Garcia-Comas, M., Funke, B., Gardini, A., Lopez-Puertas, M., Jurado-Navarro, A., von
15 Clarmann, T., Stiller, G., Kiefer, M., Boone, C. D., Leblanc, T., Marshall, B. T., Schwartz, M.
16 J., and Sheese, P. E.: MIPAS temperature from the stratosphere to the lower thermosphere:
17 Comparison of vM21 with ACE-FTS, MLS, OSIRIS, SABER, SOFIE and lidar
18 measurements, *Atmos. Meas. Tech.*, 7, 3633-3651, doi:10.5194/amt-7-3633-2014, 2014.

19 Hall, C. M.: On the influence of neutral turbulence on ambipolar diffusivities deduced from
20 meteor trail expansion, *Ann. Geophys.*, 20 (11), 1857-1862, doi: 10.5194/angeo-20-1857-
21 2002, 2002.

22 Hall, C. M., T. Aso, M. Tsutsumi, J. Höffner, F. Sigernes, and D. A. Holdsworth: Neutral air
23 temperatures at 90 km and 70°N and 78°N, *J. Geophys. Res.*, 11 (D14105), doi:
24 10.1029/2005JD006794, 2006.

25 Hall, C. M., T. Aso, M. Tsutsumi, S. Nozawa, A. H. Manson, and C. E. Meek: Letter to the
26 editor: Testing the hypothesis of the influence of neutral turbulence on the deduction of
27 ambipolar diffusivities from meteor trail expansion, *Ann. Geophys.*, 23 (3), 1071-1073, doi:
28 10.5194/angeo-23-1071-2005, 2005.

- 1 Hall, C. M., M. E. Dyrland, M. Tsutsumi, and F. J. Mulligan: Temperature trends at 90 km
2 over Svalbard, Norway (78°N 16°E), seen in one decade of meteor radar observations, *J.*
3 *Geophys. Res. – Atmos.*, 117 (D08104), doi: 10.1029/2011JD017028, 2012.
- 4 Havnes, O. and F. Sigernes: On the influence of background dust on radar scattering from
5 meteor trails, *J. Atmos. Solar-Terr. Phys.*, 67, 659-664, doi: 10.1016/j.jastp.2004.12.009,
6 2005.
- 7 Hibbins, R. E., M. J. Jarvis, and E. A. K Ford: Quasi-biennial oscillation influence on long-
8 period planetary waves in the Antarctic upper mesosphere, *J. Geophys. Res.*, 114 (D09109),
9 doi: 10.1029/2008JD011174, 2009.
- 10 Hocking, W. K.: Temperatures using radar-meteor decay times, *Geophys. Res. Lett.*, 26 (21),
11 3297-3300, doi: 10.1029/1999GL003618, 1999.
- 12 Hocking, W. K.: Radar meteor decay rate variability and atmospheric consequences, *Ann.*
13 *Geophys.*, 22 (11), 3805-3814, doi: 10.5194/angeo-22-3805-2004, 2004.
- 14 Hocking, W. K., T. Thayaparan, and J. Jones: Meteor decay times and their use in
15 determining a diagnostic mesospheric temperature-pressure parameter: methodology and one
16 year of data, *Geophys. Res. Lett.*, 24 (23), 2977-2980, doi: 10.1029/97gl03048, 1997.
- 17 Hoffmann, P., E. Becker, W. Singer, and M. Placke: Seasonal variation of mesospheric waves
18 at northern middle and high latitudes, *J. Atmos. Solar-Terr. Phys.*, 72, 1068-1079, doi:
19 10.1016/j.jastp.2010.07.002, 2010.
- 20 Hoffmann, P., M. Rapp, W. Singer, and D. Keuer: Trends of mesospheric gravity waves at
21 northern middle latitudes during summer, *J. Geophys. Res.*, 116 (D00P08), doi:
22 10.1029/2011JD015717, 2011.
- 23 Holdsworth, D. A., R. J. Morris, D. J. Murphy, I. M. Reid, G. B. Burns, and W. J. R. French:
24 Antarctic mesospheric temperature estimation using the Davis mesosphere-stratosphere-
25 troposphere radar, *J. Geophys. Res. – Atmos.*, 111 (D5), doi: 10.1029/2005jd006589, 2006.
- 26 Holmen, S. E., M. E. Dyrland, and F. Sigernes: Mesospheric temperatures derived from three
27 decades of hydroxyl airglow measurements from Longyearbyen, Svalbard (78°N), *Acta*
28 *Geophys.*, doi: 10.2478/s-11600-013-0159-4, 2013.

- 1 Holmen, S. E., M. E. Dyrland, and F. Sigernes: Long-term trends and the effect of solar cycle
2 variations on mesospheric winter temperatures over Longyearbyen, Svalbard (78°N), J.
3 Geophys. Res. – Atmos., 119, 6596-6608, doi: 10.1002/2013jd021195, 2014.
- 4 Horne, J. H., and S. J. Baliunas: A prescription for period analysis for unevenly sampled time
5 series, The Astrophysical Journal, 302, 757-763, doi: 10.1086/164037, 1986.
- 6 Jacobi, C.: Long-term trends and decadal variability of upper mesosphere/lower thermosphere
7 gravity waves at midlatitudes, J. Atmos. Solar-Terr. Phys., 118, 90-95, doi:
8 10.1016/j.astp.2013.05.009, 2014.
- 9 Kovalev, D. V., A. P. Smirnov, and Y. S. Dimant: Modeling of the Farley-Buneman
10 instability in the E-region ionosphere: a new hybrid approach, Ann. Geophys., 26, 2853-2870,
11 doi: 10.5194/angeo-26-2853-2008, 2008.
- 12 Laštovička, J., R. A. Akmaev, G. Beig, J. Bremer, J. T. Emmert, C. Jacobi, M. J. Jarvis, G.
13 Nedoluha, Y. I. Portnyagin, and T. Ulich: Emerging pattern of global change in the upper
14 atmosphere and ionosphere, Ann. Geophys., 26, 1255-1268, doi: 10.5194/angeo-26-1255-
15 2008, 2008.
- 16 Laštovička, J., S. C. Solomon, and L. Qian: Trends in the neutral and ionized upper
17 atmosphere, Space Sci. Rev., 168, 113-145, doi: 10.1007/s11214-011-9799-3, 2012.
- 18 Liu, H.-L., R. G. Roble, M. J. Taylor, W. R. Pendleton, Jr.: Mesospheric planetary waves at
19 northern hemisphere fall equinox, Geophys. Res. Lett., 28 (9), 1903-1906, doi:
20 10.1029/2000GL012689, 2001.
- 21 Lübken, F.-J.: Thermal structure of the Arctic summer mesosphere, J. Geophys. Res. –
22 Atmos., 104 (D8), 9135-9149, doi: 10.1029/1999JD900076, 1999.
- 23 Lübken, F.-J., Berger, U., and Baumgarten, G.: Temperature trends in the midlatitude summer
24 mesopause, J. Geophys. Res. Atmos., 118, 13347-13360, doi:10.1002/2013JD020576, 2013.
- 25 Lübken, F.-J. and U. von Zahn: Thermal structure of the mesopause region at polar latitudes,
26 J. Geophys. Res. – Atmos., 96 (D11), 20841-20857, doi: 10.1029/91JD02018, 1991.

1 Manabe, S. and R. T. Wetherald: The effects of doubling the CO₂ concentration on the
2 climate of a general circulation model, *J. Atmos. Sci.*, 32 (1), 3-15, doi: 10.1175/1520-
3 0469(1975)032<0003:TEODTC>2.0.CO;2, 1975.

4 Manson, A. H., C. E. Meek, J. Stegman, P. J. Espy, R. G. Roble, C. M. Hall, P. Hoffmann,
5 and Ch. Jacobi: Springtime transitions in mesopause airglow and dynamics: photometer and
6 MF radar observations in the Scandinavian and Canadian sectors, *J. Atmos. Solar-Terrr.*
7 *Phys.*, 64, 1131-1146, doi: 10.1016/S1364-6826(02)00064-0, 2002.

8 McKinley, D. W. R.: *Meteor Science and Engineering*, McGraw-Hill, New York, 1961.

9 NASA (2016): *Annual Meteorological Statistics*, National Aeronautics Space Administration,
10 http://acdb-ext.gsfc.nasa.gov/Data_services/met/ann_data.html, accessed April 2016.

11 NASA Jet Propulsion Laboratory (2015), *EOS Microwave Limb Sounder*,
12 <http://mls.jpl.nasa.gov/index-eos-mls.php>, accessed January 2015.

13 Niciejewski, R. J. and T. L. Killeen: Annual and semi-annual temperature oscillations in the
14 upper mesosphere, *Geophysical Research Letters*, 22 (23), 3243-3246, doi:
15 10.1029/95GL02411, 1995.

16 Offermann, D., P. Hoffmann, P. Knieling, R. Koppmann, J. Oberheide, and W. Steinbrecht:
17 Long-term trends and solar cycle variations of mesospheric temperatures and dynamics, *J.*
18 *Geophys. Res.*, 115, D18127, doi: 10.1029/2009JD013363, 2010.

19 Ogawa, Y., T. Motoba, S. C. Buchert, I. Häggström, and S. Nozawa: Upper atmosphere
20 cooling over the past 33 years, *Geophys. Res. Lett.*, 41, 5629-5635, doi:
21 10.1002/2014GL060591, 2014.

22 Oliver, W. L., S.-R. Zhang, and L. P. Goncharenko: Is thermospheric global cooling caused
23 by gravity waves?, *J. Geophys. Res. - Space Physics*, 118, 3898-3908, doi:
24 10.1002/jgra.50370, 2013.

25 Press, W. H., and G. B. Rybicki: Fast algorithm for spectral analysis of unevenly sampled
26 data, *Astrophysical Journal, Part 1*, 338, 277-280, doi: 10.1086/167197, 1989.

- 1 Rees, D., H. Rishbeth, and T. R. Kaiser: Winds and temperatures in the auroral zone and their
2 relations to geomagnetic activity, *Philosophical Transactions of the Royal Society of London.*
3 *Series A, Mathematical and Physical Sciences*, 271, 1217, 563-575, doi:
4 10.1098/rsta.1972.0024, 1972.
- 5 Roble, R. G. and R. E. Dickinson: How will changes in carbon dioxide and methane modify
6 the mean structure of the mesosphere and thermosphere?, *Geophys. Res. Lett.*, 16 (12), 1441-
7 1444, doi: 10.1029/GL016i012p01441, 1989.
- 8 Salby, M. L.: Rossby normal modes in nonuniform background configurations. Part I: Simple
9 fields, *Journal of the Atmospheric Sciences*, 38 (9), 1803-1826, doi: 10.1175/1520-
10 0469(1981)038<1803:RNMINB>2.0.CO;2, 1981a.
- 11 Salby, M. L.: Rossby normal modes in nonuniform background configurations. Part II:
12 Equinox and solstice conditions, *Journal of the Atmospheric Sciences*, 38 (9), 1827-1840, doi:
13 10.1175/1520-0469(1981)038<1827:RNMINB>2.0.CO;2, 1981b.
- 14 Scargle, J. D.: Studies in astronomical time series analysis. II. Statistical aspects of spectral
15 analysis of unevenly spaced data, *The Astrophysical Journal*, 263, 835-853, doi:
16 10.1086/160554, 1982.
- 17 Schmidt, H., G. P. Brasseur, M. Charron, E. Manzini, M. A. Giorgetta, and T. Diehl: The
18 HAMMONIA Chemistry Climate Model: Sensitivity of the mesopause region to the 11-year
19 solar cycle and CO₂ doubling, *J. Climate*, 19 (16), 3903-3931, doi: 10.1175/JCLI3829.1,
20 2006.
- 21 Shepherd, M. G., P. J. Espy, C. Y. She, W. Hocking, P. Keckhut, G. Gavrilieva, G. G.
22 Shepherd, and B. Naujokat: Springtime transition in upper mesospheric temperature in the
23 northern hemisphere, *J. Atmos. Solar-Terr. Phys.*, 64, 1183-1199, doi: 10.1016/S1364-
24 6826(02)00068-8, 2002.
- 25 Shepherd, M. G., Y. J. Rochon, D. Offermann, M. Donner, and P. J. Espy: Longitudinal
26 variability of mesospheric temperatures during equinox at middle and high latitudes, *J.*
27 *Atmos. Solar-Terr. Phys.*, 66, 463-479, doi: 10.1016/j.jastp.2004.01.036, 2004.

1 Stray, N. H., R. J de Wit, P. J. Espy, and R. E. Hibbins: Observational evidence for temporary
2 planetary wave forcing of the MLT during fall equinox, *Geophys. Res. Lett.*, 41, 6281-6288,
3 doi: 10.1002/2014GL061119, 2014.

4 Taylor, M. J., W.R. Pendleton, Jr., H.-L. Liu, C. Y. She, L. C. Gardner, R. G. Roble, and V.
5 Vasoli: Large amplitude perturbations in mesospheric OH Meinel and 87-km Na lidar
6 temperatures around the autumnal equinox, *Geophys. Res. Lett.*, 28 (9), 1899-1902, doi:
7 10.1029/2000GL012682, 2001.

8 Tiao, G. C., G. C. Reinsel, D. Xu, J. H. Pedrick, X. Zhu, A. J. Miller, J. J. DeLuisi, C. L.
9 Mateer, and D. J. Wuebbles: Effects of autocorrelation and temporal sampling schemes on
10 estimates of trend and spatial correlation, *J. Geophys. Res. – Atmos.*, 95 (D12), 20507-20517,
11 doi: 10.1029/JD095iD12p20507, 1990.

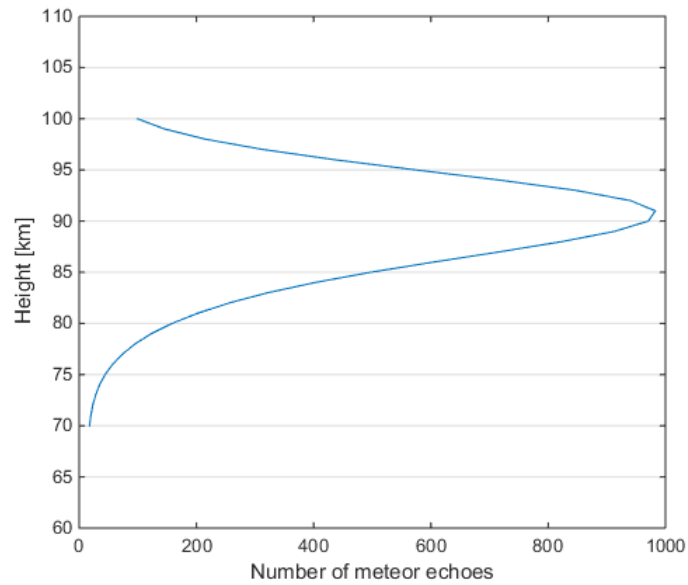
12 von Savigny, C.: Variability of OH(3-1) emission altitude from 2003 to 2011: Long-term
13 stability and universality of the emission rate-altitude relationship, *J. Atmos. Sol.-Terr. Phys.*,
14 127, 120-128, <http://dx.doi.org/10.1016/j.astp.2015.02.001>, 2015.

15 Walterscheid, R. L.: Dynamical cooling induced by dissipating internal gravity waves,
16 *Geophys. Res. Lett.*, 8, 1235-1238, doi: 10.1029/GL008i012p01235.

17 Weatherhead, E. C., G. C. Reinsel, G. C. Tiao, X.-L. Meng, D. Choi, W.-K. Cheang, T.
18 Keller, J. DeLuisi, D. J. Wuebbles, J. B. Kerr, A. J. Miller, S. J. Oltmans, and J. E. Frederick:
19 Factors affecting the detection of trends: Statistical considerations and applications to
20 environmental data, *J. Geophys. Res.* 103 (D14), 17149-17161, doi: 10.1029/98JD00995,
21 1998.

22 Winick, J. R., P. P. Wintersteiner, R. H. Picard, D. Esplin, M. G. Mlynczak, J. M. Russell III,
23 and L. L. Gordley: OH layer characteristics during unusual boreal winters of 2004 and 2006,
24 *J. Geophys. Res.*, 114, A02303, doi: 10.1029/2008JA013688, 2009.

25 Yigit, E. and Medvedev, A. S.: Heating and cooling of the thermosphere by internal gravity
26 waves, *Geophys. Res. Lett.*, 36, L14807, doi: 10.1029/2009GL038507
27

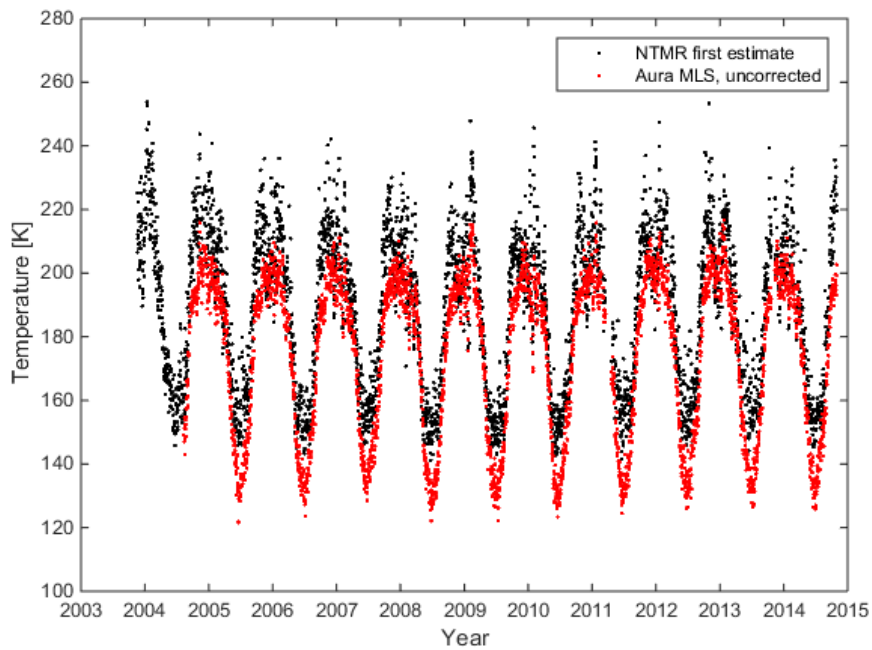


1

2 Figure 1: Vertical distribution of the occurrence of meteor echoes over Tromsø, averaged over
 3 height between 2003 and 2014. The peak occurrence height is just over 90 km altitude.

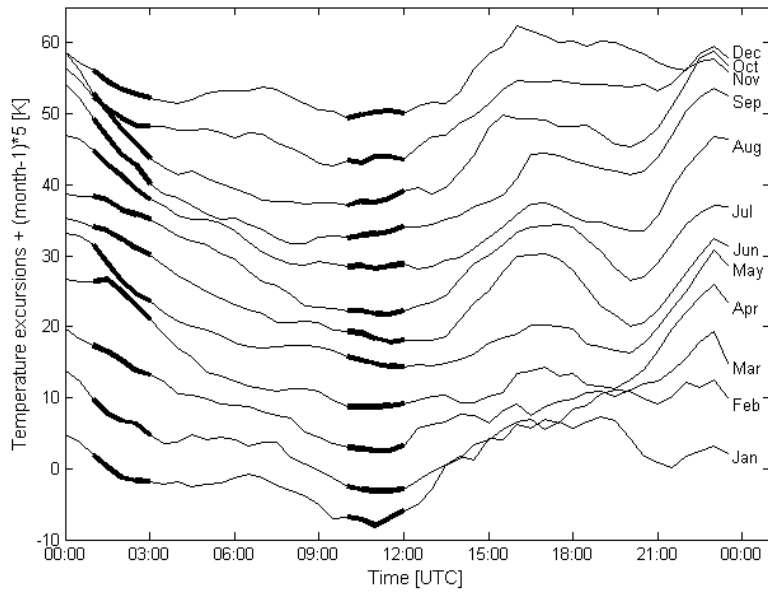
4

5

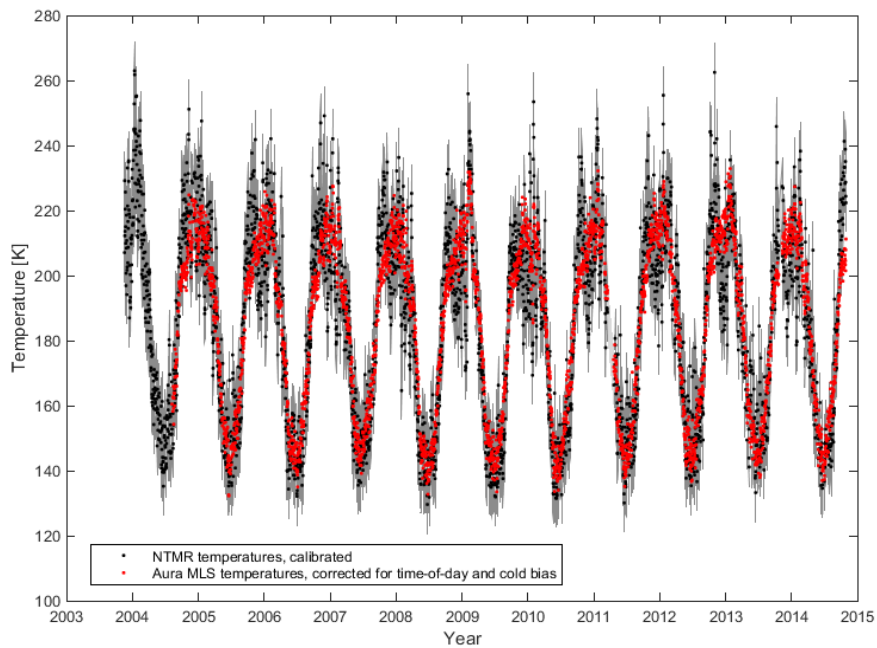


6

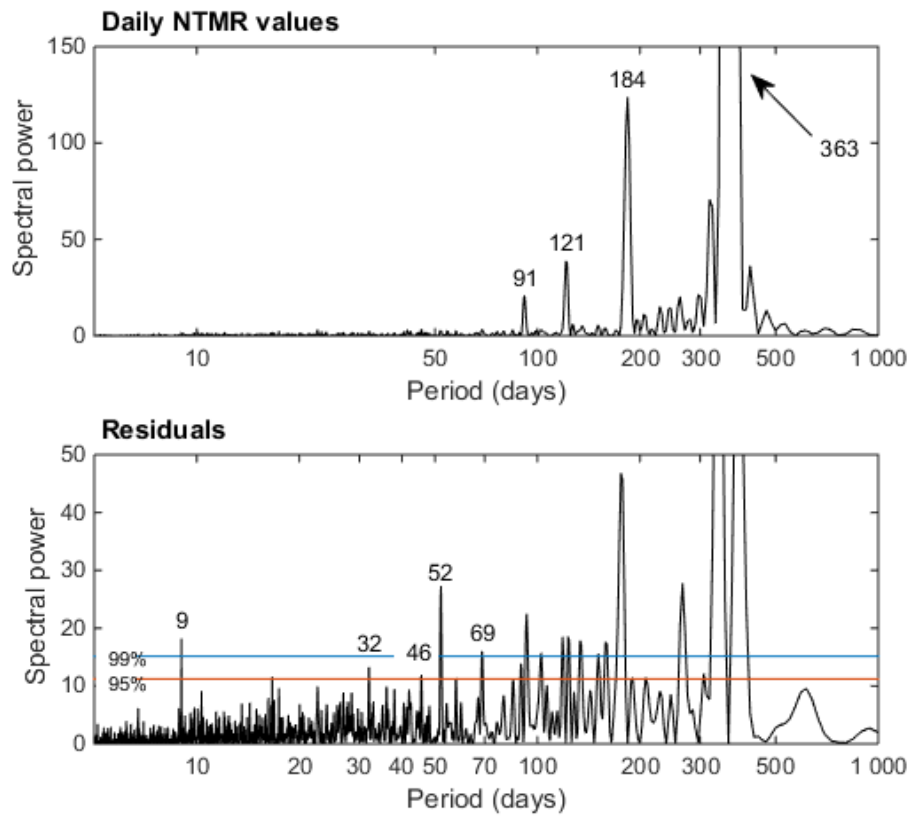
7 Figure 2. Daily values of NTMR temperatures derived from Eqs. (1) and (2), before
 8 correction for high D_a , plotted together with Aura MLS temperatures, before applying any
 9 corrections.



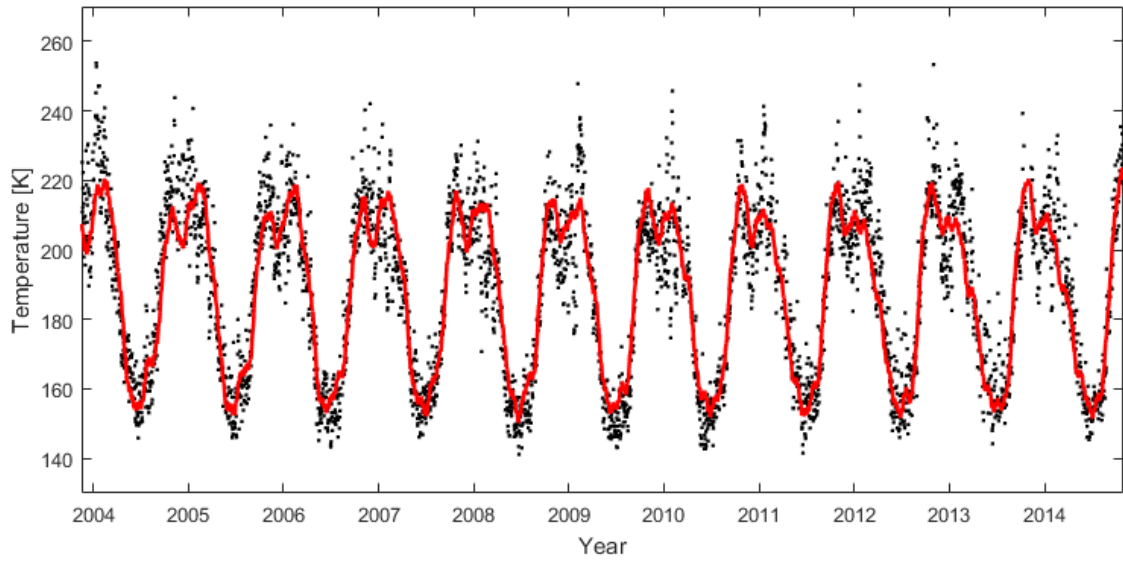
1
 2 Figure 3. Monthly averages of diurnal temperature variation derived from NTMR after
 3 correction for high D_a at 90 km altitude. For clarity time series are displaced by 5 K per
 4 month subsequent to January. The time of day corresponding to when Aura makes
 5 measurements over Tromsø (01-03 UTC and 10-12 UTC) is highlighted.



6
 7 Figure 4. Daily values of MLS-calibrated NTMR temperatures plotted together with Aura
 8 MLS temperatures corrected for cold and time-of-day bias. The overall calibration uncertainty
 9 is indicated by the grey shading.



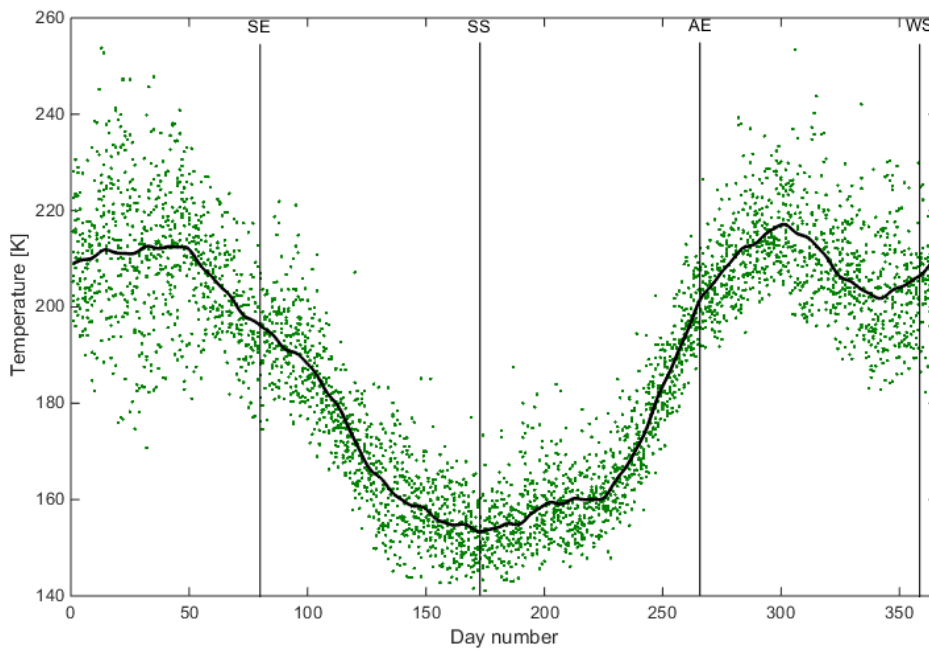
1
 2 Figure 5: Upper panel: Lomb-Scargle periodogram for daily NTMR temperatures from 2003
 3 to 2014. The y axis has been truncated for clarity. Lower panel: Periodogram for residuals
 4 after fitting sinusoids for the four largest peaks from the upper panel. Peaks significant at
 5 better than 95 % are marked with numbers corresponding to period.



1

2 Figure 6. MLS-corrected NTMR daily temperatures (black dots) and the least-squares fit of
 3 the average, trend and periodic components (red curve).

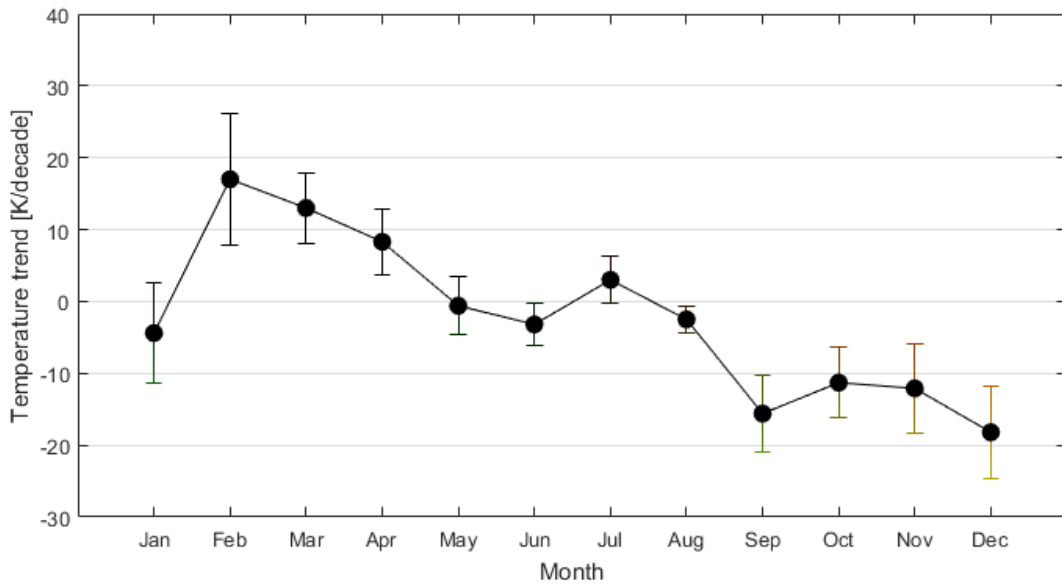
4



5

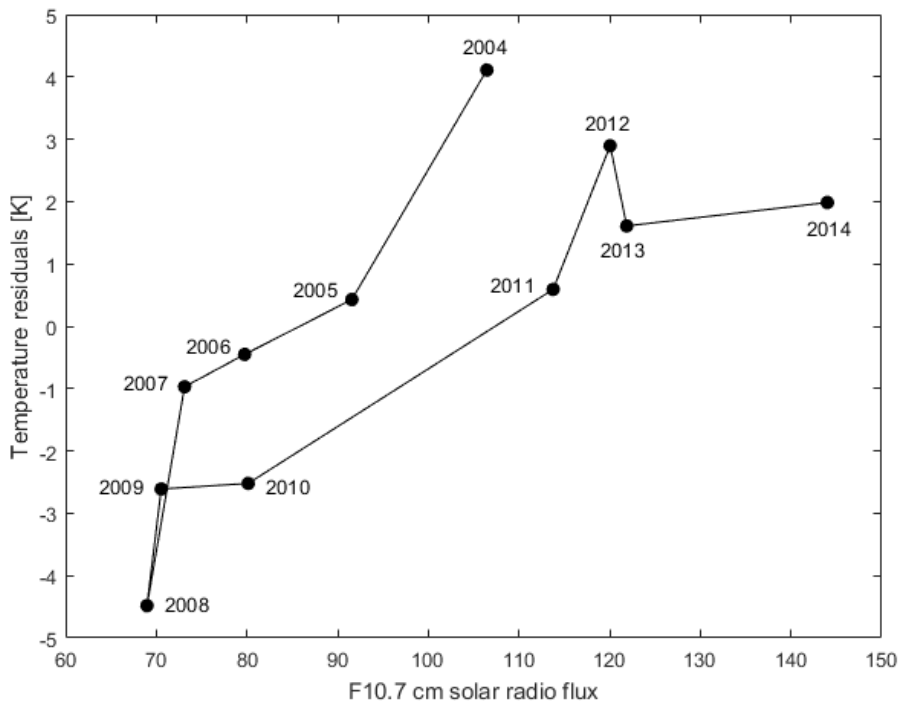
6 Figure 7: Superposed-epoch analysis of daily MLS-corrected NTMR temperatures. The
 7 smooth, black line is the composite fit of all periodic components listed in Table 2. Spring and
 8 autumn equinoxes and winter and summer solstice are marked SE, AE, WS and SS,
 9 respectively.

1



2

3 Figure 8. Monthly temperature trends at 90 km altitude over Tromsø. Standard deviations are
4 given as error bars.



5

6 Figure 9. Yearly values of F10.7 cm solar radio flux plotted against yearly averaged
7 temperature fit residuals. Year 2003 is left out of the figure due to the data coverage (only
8 data for November and December).

Month	Jan	Feb	Mar	Apr	May	Jun	Jul	Aug	Sep	Oct	Nov	Dec
Aura bias (K)	-6.3	-6.5	-3.3	-0.08	-0.5	-0.6	-1.4	-1.3	-2.7	-3.5	-3.9	-4.6
σ (K)	3.2	4.7	6.0	8.1	6.6	7.1	7.5	6.7	6.0	5.3	2.6	1.8

1 **Table 1:** Bias/overestimate expected from Aura monthly averages due to that Aura MLS only measures between
2 01 UTC and 03 UTC, and between 10 UTC and 12 UTC.

3

Periodic component (days)	Amplitude (K)
363	21.5 ± 0.4
184	6.5 ± 0.4
121	3.8 ± 0.4
91	2.9 ± 0.4
69	1.2 ± 0.4
52	1.5 ± 0.4
46	1.1 ± 0.4
32	0.9 ± 0.4
9.0	1.0 ± 0.4

4 **Table 2:** Periodic components found in data using Lomb-Scargle periodogram analysis. All components were
5 identified as better than the 99% significance level, except for the 32 day harmonic, which was significant at the
6 95 % level. Amplitudes are given with 95 % confidence bounds.